OPTIMAL DESIGN OF VECTORED THRUST EVTOL ROTOR BLADES

Tianheng Yao Yiran Gong Liangjun Li Shuai Zhang Chen Jiang* Haowen Wang

School of Aerospace Engineering, Tsinghua University, Beijing 100084, China

Abstract

This paper employs a comprehensive analysis code to investigate the effects of key parameters on variable-speed rotors. The feasibility of reducing tip speed to achieve noise mitigation is validated; however, it is also shown that this approach may compromise the wind resistance capability of eVTOLs. This paper presents a comprehensive optimization method focusing on aerodynamics, noise reduction, and wind resistance capability to overcome challenges induced by wind disturbances during the landing phase of vectored thrust eVTOLs. The method decouples the optimization of rotor tip speed from that of blade geometry to improve computational efficiency and accelerate the optimization process. Using the proposed method, two sets of optimizations were conducted. Result A, which does not account for wind resistance capability, shows varying degrees of improvement or preservation in both aerodynamic and acoustic performance during hover and forward flight. Result B, optimized with the inclusion of a wind resistance coefficient, sacrifices part of the aerodynamic and acoustic performance in forward flight in exchange for a lower thrust fluctuation rate and lower gust reduced frequency, indicating enhanced wind resistance capability.

1. NOTATION

Symbols

c_n	Chord distribution
k_g	Gust reduced frequency
num_b	Number of blades
p_β	elliptic function hyperparameters
q_β	elliptic function hyperparameters
R_t	Blade radius
R_h	Blade root radius
T_{hov}	Thrust per rotor in hover
T_{cr}	Thrust per rotor in forward flight
SPL	Sound pressure level
SPL_A	A-weighted sound pressure level
V_{thov}	Tip speed in hover
V_{tcr}	Tip speed in forward flight
β_0	Blade pitch angle
β_h	Blade root twist
β_n	Twist distribution
β_t	Tip twist
η	Propeller efficiency
η_n	Spanwise position
θ_{hov}	Collective pitch in hover
θ_{cr}	Collective pitch in forward flight
σ	Rotor solidity
Ω	Rotor rotational speed

Acronyms

CFD	Computational Fluid Dynamics
eVTOL	electric Vertical Take-Off and Landing
FM	Figure of Merit
FW-H	Ffowcs Wiliams-Hawkings
SPL	Sound Pressure Level

2. INTRODUCTION

In recent years, electric Vertical Take-Off and Landing (eVTOL) technology has experienced rapid global development. eVTOLs offer distinct advantages in safety and noise reduction compared to traditional aircraft. Their low noise and emissions position them as key players in addressing environmental pollution and urban traffic congestion.

Among various configurations, vectored thrust eVTOLs stand out for their superior cruise efficiency, speed, and range. The rotor, the primary source of both thrust and noise, plays a crucial role in the aircraft's overall performance. For vectored thrust eVTOLs, it is imperative to evaluate rotor performance across multiple flight modes, including helicopter mode, airplane mode, and the transitional tilting phase, imposing stringent rotor blade design requirements.

Designs featuring low tip speeds and high solidity can substantially reduce rotor noise while maintaining high efficiency—a principle widely adopted in vectored thrust eVTOLs. However, this approach introduces new challenges. Firstly, low tip speeds heighten the rotor's sensitivity to winds; even at modest wind speeds, significant fluctuations in the blades' effective angle of attack can occur, compromising flight stability. Secondly, increased solidity results in a larger moment of inertia, adversely affecting acceleration performance and response bandwidth. Therefore, when designing vectored thrust eVTOLs, it is essential to account for the impacts of low tip speeds and high solidity.

Several studies have highlighted the significant aerodynamic and control effects of gusts on multirotor systems. Bo Li et al. (Ref. 1) conducted a five-year measurement of urban wind conditions at altitudes ranging from 8 to 280 meters in Beijing. The results show that wind speeds below 4 m/s are predominant at a height of 47 meters. However, above 140 meters, the occurrence probability of wind speeds exceeding 6 m/s increases significantly. Furthermore, wind below 10 Hz could be observed throughout the measurement period. Jones et al.（Ref. 2）pointed out that small-scale unmanned aerial vehicles (UAVs) and Advanced Air Mobility operations in low-level urban environments, nap-of-the-earth, and shipboard operations will encounter gusts on the order of vehicle reference scales with magnitudes that will induce nonlinear, separated flows. Narayanan et al.（Ref. 3）used the free vortex method to study the time and frequency domain of thrust, spanwise angle of attack distribution, and the rotor wake structure across the gust event. The study has shown that gusts will reduce the effective angle of attack, leading to a decrease in lift. An overshoot in thrust is often observed at the end of a gust event. Moreover, gusts may intensify blade–vortex interactions (BVI) between the wakes of different rotors. In summary, gusts are a common phenomenon in urban low-altitude environments and have a non-negligible impact on the performance and controllability of eVTOLs. Therefore, the influence of wind should be taken into account in the rotor design process.

Numerous studies have explored rotor blade shape optimization to improve performance. Several researchers(Refs. 4,5) have adopted high-fidelity methods such as CFD and CSD to get rotor performance, which is a computationally expensive way and not suitable for optimal design. Clarke(Ref. 6) et al. present an inexpensive but suitably accurate approach for designing low-noise rotors for vertical and short take-off and landing aircraft. Wilke(Ref. 7) et al. have joined forces to cooperate on optimizing helicopter rotor blades. The cooperation approved that most simulation methodologies are useful for rotor blades in various flight conditions. In summary, previous rotor blade optimization methods(Refs. 9-13) for eVTOLs face two key issues: previous studies have not comprehensively considered multiple performance metrics of variable-speed rotors across different flight conditions, nor have they examined the impact of low tip speeds and high solidity on wind resistance.

This paper utilizes computational analysis to define the range and constraints of the optimization parameters. A comprehensive optimization method is presented focusing on aerodynamics, noise reduction, and wind resistance capability of variable-speed rotors. The general conclusions of this paper are drawn from the comparative analysis of the various optimization outcomes.

3. COMPUTATIONAL METHODS

After evaluating both computational speed and result accuracy, this paper employs the following method to calculate rotor performance:

3.1 Dynamics

This paper uses a multi-body dynamics model for tiltrotor based on the second class of Lagrange equations. The generalized coordinates and velocities in the second class of Lagrange equations are directly associated with the system's motion state, which avoids the need to deal with redundant constraint equations in the first class of Lagrange equations. The structural model is derived from moderately deformed beam theory, with the blade discretized by elements of 5 nodes and 15 degrees of freedom.

3.2 Aerodynamics

The free-wake methods are a class of medium-fidelity vortex methods. It is formulated under the Lagrangian framework based on the assumptions of incompressibility and inviscid flow. This method accounts for both the self-induced motion of the wake and its distortion effects. Compared with computational fluid dynamics (CFD) methods, it offers significantly higher computational efficiency while maintaining greater accuracy than traditional inflow models. Considering the above advantages, the free-wake method is employed in this study to model the rotor wake and to perform the optimization design of rotor blades.

The rotor wake consists of a series of vortices shed from the blade. The wake region within 30 degrees of the blade azimuth is considered the near wake, while beyond this range, the wake forms a large tip vortex. The circulation in the near wake can be computed using the bound vortices derived from the Weissinger-L lifting line theory, while the circulation strength of the tip vortex corresponds to the maximum circulation of the blade. The governing equations of the free-wake method are as follows (Eq. 1):

$$\begin{cases} \frac{d\mathbf{r}}{dt} = \mathbf{V}(\mathbf{r}) \\ \mathbf{r} = \mathbf{r_0} \quad t = 0 \end{cases} \tag{1}$$

Where $\mathbf{r}$ is the position of a given point on the wake filament, $\mathbf{r_0}$ is its initial position and $\mathbf{V}(\mathbf{r})$ is the local flow velocity at that point. $\mathbf{r}$ can be expressed as a function of the blade azimuth location (ψ) and the wake-age (ζ); therefore, Eq. 1 can be rewritten as:

$$\begin{cases} \frac{d\mathbf{r}}{d\psi} + \frac{d\mathbf{r}}{d\zeta} = \frac{\mathbf{V}(\mathbf{r})}{\Omega} \\ \mathbf{r} = \mathbf{r_0} \quad t = 0 \end{cases} \tag{2}$$

Eq. 2 needs to be discretized to obtain a numerical solution. This study employs a second-order predictor-corrector strategy (PC2B), which introduces implicit numerical damping and enhances numerical stability for discretizing the wake governing equation. Eq. 3 can be derived by PC2B.

$$\mathbf{r}_{i+1,j+1} = \frac{(2\Delta\psi - 3\Delta\zeta)}{2\Delta\psi}\mathbf{r}_{i+1,j} + \frac{(2\Delta\psi + \Delta\zeta)}{2\Delta\psi}\mathbf{r}_{i,j} - \frac{\Delta\zeta}{2\Delta\psi}\mathbf{r}_{i-2,j} - \mathbf{r}_{i,j+1} + \frac{2\Delta\zeta}{\Omega} \tag{3}$$

The induced velocity at a given point can be calculated by integrating along the vortex filament using the Biot–Savart law Eq. 4.

$$\mathbf{V}(\mathbf{r}) = \frac{\Gamma}{4\pi}\int \frac{d\mathbf{l} \times \mathbf{r}}{|\mathbf{r}^3|} = \frac{\Gamma}{4\pi}\left[\mathbf{l} \cdot \left(\frac{\mathbf{R_2}}{|\mathbf{R_2}|} - \frac{\mathbf{R_1}}{|\mathbf{R_1}|}\right)\right]\frac{\mathbf{l} \times \mathbf{R_2}}{|\mathbf{l} \times \mathbf{R_2}|^2} \tag{4}$$

For points in close proximity to the vortex filament, the use of the Biot–Savart law may result in singularities. The semi-empirical Vatistas model Eq. 5 is employed to compute the induced velocity under such conditions in this study. Additionally, the Squire vortex core dissipation model Eq. 6 is adopted to incorporate the influence of viscous diffusion.

$$\mathbf{V}(\mathbf{r}) = \frac{\Gamma\mathbf{r}}{4\pi(r_c^4 + \mathbf{r}^4)^{0.5}} \tag{5}$$

$$r_c(\zeta) = \sqrt{4\alpha\delta v(\frac{\zeta + \zeta_0}{\Omega})} \tag{6}$$

3.3 Aeroacoustics

Following Lighthill's acoustic analogy, and under the assumptions of negligible viscous effects on sound propagation and absence of mass sources or sinks in the flow field, the governing equations(Eqs. 7, 8) for inviscid fluid motion without external forces can be derived from the Euler equations.

$$\frac{\partial\rho}{\partial t} + \frac{\partial(\rho u_i)}{\partial x_i} = 0 \tag{7}$$

$$\frac{\partial\rho u_i}{\partial t} + \frac{\partial\rho u_i u_j}{\partial x_j} = -\frac{\partial p}{\partial x_j} \tag{8}$$

To incorporate the influence of solid boundaries, the continuity and momentum equations are reformulated using generalized Heaviside and Dirac delta functions, where $f(x,t) < 0$ denotes the interior of a moving solid body and $f(x,t) > 0$ corresponds to the exterior region. This formulation forms the basis of aeroacoustic equations for sound radiation from solid surfaces.

$$H(f) = \begin{cases} 1, f(x,t) > 0 \\ 0, f(x,t) < 0 \end{cases} \tag{9}$$

$$\delta(f) = \frac{\partial H(f)}{\partial f} \quad (10)$$

Applying the impermeability condition on the solid surface, the Ffowcs Williams–Hawkings (FW-H) equation (Eq. 11) can be derived.

$$\Box^2 p' = \frac{\partial}{\partial t}[\rho_0 v_n \delta(f)] - \frac{\partial}{\partial x_j}[l_i \delta(f)] + \frac{\partial^2}{\partial x_i x_j}[H(f) T_{ij}] \quad (11)$$

By introducing the free-space Green's function, the time-domain integral formulation of the Ffowcs Williams–Hawkings (FW-H) equation can be derived, commonly known as Farassat's 1A formulation(Eqs. 12, 13).

$$4\pi p_T'(x,t) = \int_{f=0} \left[\frac{\rho_0 \dot{v}_n}{r(1-M_r)^2} + \frac{\rho_0 v_n \hat{r}_i \dot{M}_i}{r(1-M_r)^3}\right]_{ret} dS + \int_{f=0} \left[\frac{\rho_0 c v_n (M_r - M^2)}{r^2(1-M_r)^3}\right]_{ret} dS \quad (12)$$

$$4\pi p_L'(x,t) = \int_{f=0} \left[\frac{\dot{p}cos\theta}{cr(1-M_r)^2} + \frac{\hat{r}_i \dot{M}_i p cos\theta}{cr(1-M_r)^3}\right]_{ret} dS + \int_{f=0} \left[\frac{p(cos\theta - M_i n_i)}{r^2(1-M_r)^2} + \frac{(M_r - M^2) p cos\theta}{r^2(1-M_r)^2}\right]_{ret} dS \quad (13)$$

Since the Farassat's 1A formulation avoids differentiation of the integral terms, it simplifies the numerical procedure and is more amenable to computational implementation. Accordingly, it is employed in this study for aeroacoustic calculations.

4. PARAMETERS ANALYSIS

The rotor of a vectored-thrust eVTOL differs from traditional helicopter rotors in that it typically operates in an axial flow state and has the capability to change both pitch and rotational speed. Consequently, principles applicable to fixed-speed rotors may not be directly relevant. Therefore, it is essential to consider variables such as collective pitch and tip speed to evaluate their influence on rotor performance parameters. This paper is based on a tiltrotor eVTOL configuration equipped with six rotors. Each rotor consists of a 1.5-meter-diameter rotor system composed of five Advanced Technology Blades (ATB). The influence of various parameters on rotor performance is investigated.

4.1 Tip Speed

The tip speed of the rotor is a critical design parameter. The use of electric motors provides a broader design space for rotor tip speed, but also increases the complexity of the design process. For tiltrotor eVTOLs, it is necessary to design variable rotational speeds and their corresponding ranges to accommodate different flight conditions. Accordingly, this study investigates the effect of tip speed on rotor performance under the condition of constant thrust.

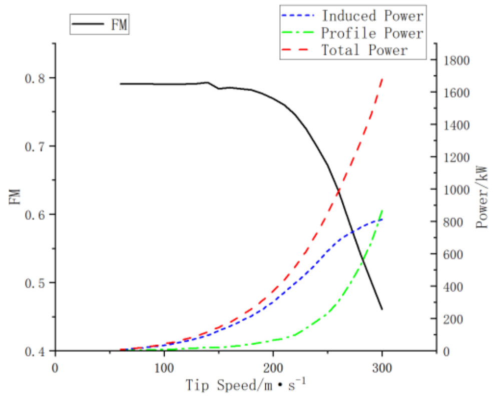

Figure 1: FM and Power Characteristics of Rotor Systems in Helicopter Mode: Variation with Tip Speed

Specifically, the impact of rotor tip speed on figure of merit (FM) was evaluated at a fixed collective pitch angle. The results show that FM remains relatively high at low tip speeds; however, once the tip speed exceeds 200 m/s, FM decreases sharply. As shown in Fig.1, this degradation is attributed to a rapid increase in profile power with increasing tip speed, whereas the growth of induced power becomes less significant, leading to a decline in FM.

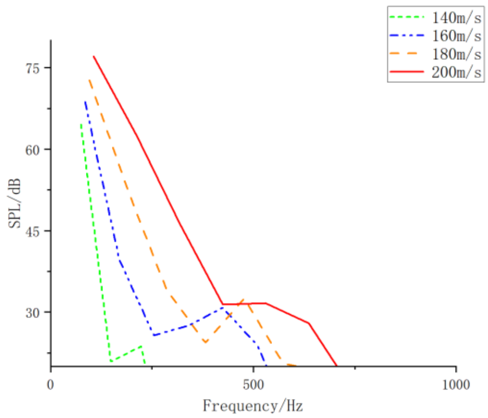

Figure 2: Overall SPL spectra at different rotor tip speeds

Rotor noise is highly sensitive to tip speed. Fig. 2 presents the sound pressure level (SPL) spectra of total noise at various tip speeds, while maintaining identical thrust. As the tip speed decreases, the SPL decreases across all frequency bands, and the dominant noise components shift toward lower frequencies. The A-weighted sound pressure level (A-weighted SPL), which accounts for the frequency-dependent sensitivity of human hearing, is widely adopted as a noise evaluation metric and will be used in the subsequent optimization process of this study. When the rotor tip speed drops below 170 m/s, the noise spectrum becomes concentrated below 600 Hz, whereas the A-weighting function assigns greater weight to frequencies above 737.9 Hz. Therefore, reducing the tip speed below 170 m/s is more effective in minimizing A-weighted noise.

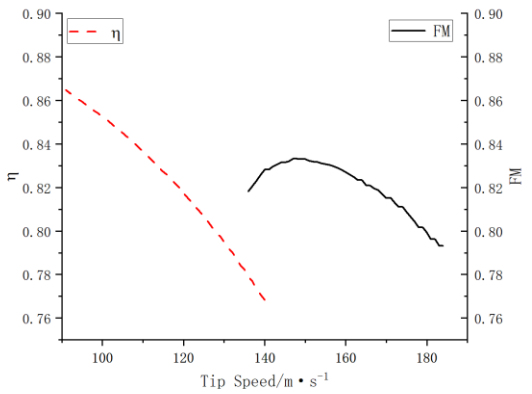

Figure 3: Variation of FM and η with rotor tip speed

The variation of rotor FM with tip speed under a constant thrust of 4500 N is shown in Fig. 3. For the rotor tested in this study, the maximum FM is achieved at a tip speed of 148 m/s. In airplane mode, when the generated thrust is maintained at 1000 N, the propeller efficiency decreases with increasing tip speed. This occurs because, while the propulsive power remains nearly constant under fixed thrust, achieving a higher tip speed requires a greater total power input, which ultimately leads to reduced propeller efficiency.

4.2 Collective pitch

As shown in Fig. 4, in helicopter mode, the FM exhibits similar trends across different tip speeds with respect to variations in collective pitch. Within the range of 10° to 20°, the FM remains above 0.8; however, outside this range, it declines rapidly.

Fig.5 illustrates that in airplane mode, propeller efficiency gradually decreases with increasing collective pitch. When the increase in collective pitch causes the angle of attack to exceed a critical value, the propeller efficiency begins to drop sharply, and this threshold is reached more easily at higher tip speeds.

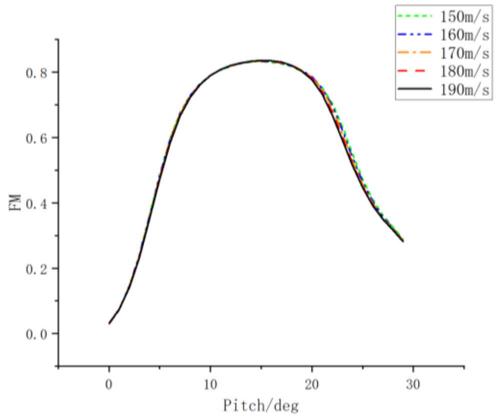

Figure 4: Variation of FM with collective pitch at different rotor tip speeds.

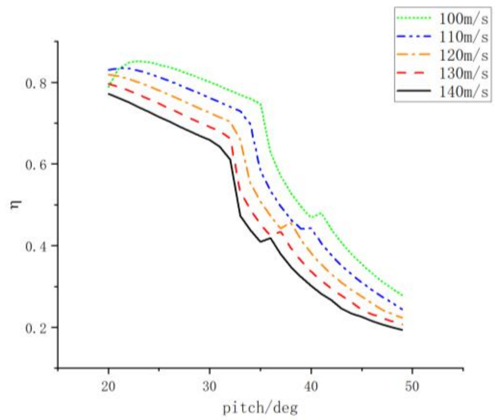

Figure 5: Variation of η with collective pitch at different rotor tip speeds.

As shown in Fig. 6, in helicopter mode, when the rotor lift is maintained at a constant 4500 N, the rotor achieves maximum FM at a collective pitch of 15°. In airplane mode, under a constant thrust of 1000 N, propeller efficiency increases as the collective pitch decreases. Moreover, when maintaining constant thrust, increasing the collective pitch typically results in a reduction in tip speed. Considering the combined effect of these two factors, the propeller efficiency is improved.

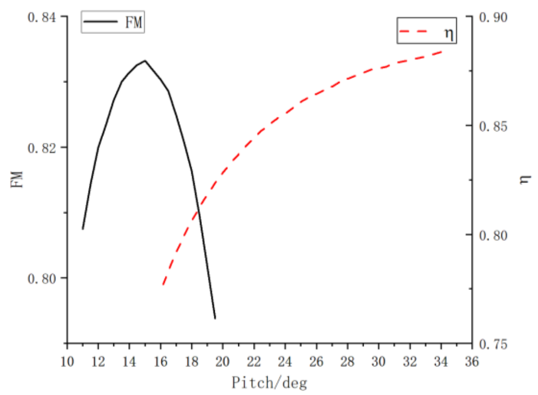

Figure 6: Variation of FM and η with collective pitch speed.

In summary, the variation of collective pitch and tip speed collectively governs rotor performance. An appropriate combination tailored to the specific blade geometry should be identified through a comprehensive design trade-off.

4.3 Gust

When an eVTOL operates at low speeds with reduced tip speed, wind can significantly affect its control. A simulation was conducted to analyze an eVTOL during descent, flying at 30 m/s with the rotor axis tilted forward by 30°. Fig. 7 illustrates the impact of lateral wind on the effective angle of attack at 75% rotor radius (R) across different tip speeds. A 10 m/s wind can induce a 1.6° variation in the effective angle of attack. Implementing an appropriate twist distribution may allow blade segments to adjust lift generation in response to wind disturbances, thereby maintaining a nearly constant total rotor force. Therefore, it is essential to establish a maximum thrust fluctuation rate limit during rotor design to ensure adequate wind resistance and maintain flight stability.

eVTOLs typically regulate rotor thrust through adjustments in blade pitch and rotational speed, making rotor acceleration and deceleration performance crucial. However, increasing rotor solidity elevates the blade's moment of inertia, hindering rapid speed changes. A 50% increase in rotor solidity leads to a 56% reduction in angular acceleration under constant torque conditions. To maintain the original angular acceleration, the motor must provide 2.25 times the previous torque, significantly increasing the load on the electric motor. Therefore, the rotor solidity should be constrained to enhance the rotor's controllability under varying inflow conditions.

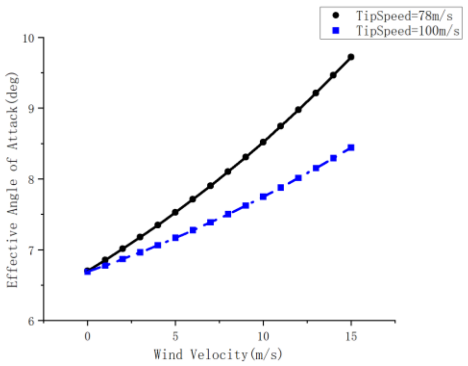

Figure 7: Variation of Effective Angle of Attack with Wind Velocity(@ 75% R)

5. Optimal Design Method

5.1 Optimize parameters and constraints

This study focuses on the optimization design of rotors for a six-rotor vectored-thrust eVTOL configuration. Based on the preceding analysis, a preliminary selection of key parameters is made. The chosen rotor design parameters are summarized in Table 1.

Table 1: Selected Rotor Parameters

Parameters	value
R_t	1.5m
R_h	0.175m
num_b	5
Airfoil Distribution	ATB Airfoil Distribution

In the conventional approach, chord and twist distributions are defined by specifying values at each blade segment. However, this method significantly increases the number of design variables, which not only slows down the optimization process but also increases the risk of convergence to local optima. To reduce the number of parameters, the chord distribution is parameterized using a cubic polynomial (Eq. 14), while the twist distribution is represented by a conic curve with a linear deviation term (Eq. 15), following the method in Ref. 6.

$$c_n = a\eta_n^3 + b\eta_n^2 + c\eta_n + d \qquad (14)$$

$$\beta_n = \beta_h\left(1 - \eta_n^{p_\beta}\right)^{q_\beta} + \beta_t\eta_n + \beta_0 \qquad (15)$$

A cosine spacing function (Eq. 16) is adopted to refine the blade segmentation to accurately capture the nonlinear spanwise variations of blade circulation and loading. This approach enhances the fidelity of aerodynamics and aeroacoustics calculations.

$$\eta_n = \frac{R_h}{R_t} + \left(1 - \frac{R_h}{R_t}\right)\cos\left(\frac{\pi}{2}\cdot\frac{(N+1-n)}{N}\right) \qquad (16)$$
$$, n = 1,2,\dots,N+1$$

Following the analysis presented in Section 4, the optimization parameters and their variable ranges are defined as shown in Table 2.

Constraints on lift and thrust under both hover and forward flight conditions are imposed to ensure that the rotor provides sufficient vertical and horizontal force. In order to obtain physically reasonable chord and twist distributions, corresponding design parameters are also constrained. Limits are further applied to key performance metrics to prevent the optimization from achieving improvements in one metric at the expense of others. Additionally, a constraint on the thrust fluctuation rate ($\Delta T\ /\ T$) under a 10 m/s wind is introduced to ensure adequate wind resistance capability of the rotor. The final set of constraints is summarized in Table 3.

Table 2: Optimization design variables and their ranges

Parameters	Bounds [lower upper]
$V_{thov}/m\cdot s^{-1}$	[100,160]
θ_{hov}/deg	[5,20]
$V_{tcr}/m\cdot s^{-1}$	[60,120]
θ_{cr}/deg	[15,30]
a	[-0.5,-0.05]
b	[0.01,0.03]
c	[0.01,0.1]
d	[0.1,0.2]
β_h/deg	[10,30]
β_t/deg	[-10,0]
β_0/deg	[0,5]
p_β	[0.25,2]
q_β	[0.25,2]

Table 3: Constraints applied in the optimization

Parameters	Constrains	Description
T_{hov}	$=T_{hov}^*$	Lift per rotor in hover
T_{cr}	$=T_{cr}^*$	Thrust per rotor in forward flight
$\Delta T_{hov}/T_{hov}$	<0.1	Constraint on lift variation under gust
$\Delta T_{cr}/T_{cr}$	<0.1	Constraint on lift variation under gust
$a+b+c+d$	≥ 0.03	Eliminate unreasonable distributions
p_β/q_β	≥ 0.5	Eliminate unreasonable distributions
FM	≥ 0.8	
η_{cr}	≥ 0.85	
k_{rd}	<0.005	

5.2 Objective Function

The rotor is required to meet aerodynamic, acoustic, and wind resistance capabilities across multiple flight modes, leading to a multi-objective optimization problem. However, conventional multi-objective optimization typically results in a Pareto front, from which the final design must still be selected based on empirical judgment. To address this, expert knowledge is incorporated directly into the optimization phase, and a problem-specific objective function is formulated to transform the multi-objective problem into a single-objective one, thereby reducing the complexity of the optimization process. A weighted-exponential sum approach is adopted as the objective function(Eq. 17).

$$f(\mathbf{x})=\sum_{i=1}^{m}w_i\left|\frac{f_i(\mathbf{x})-y_i^{goal}}{y_i^{goal}}\right| \tag{17}$$

To achieve high performance in both helicopter and airplane modes, this study integrates the performance metrics of both modes into a single objective function using a weighted approach. The objective function is formulated as follows(Eq. 18):

$$\begin{aligned}f(x)=\alpha_{aero}f_{\text{aero}}+\alpha_{acoustic}f_{acoustic}\\+(1-\alpha_{aero}-\alpha_{acoustic})f_{wind}\end{aligned} \tag{18}$$

The aerodynamic performance optimization must simultaneously address the operational requirements of both hover and forward flight conditions. For quantitative evaluation, the figure of merit and propeller efficiency are employed as the respective performance metrics for these two flight regimes. Given that higher efficiency values correspond to superior aerodynamic performance, the objective function for this component is formulated using the percentage by which the achieved efficiency exceeds the target value, rather than employing absolute differences. The mathematical representation of this aerodynamic objective function is presented below(Eq. 19):

$$\begin{aligned}f_{aero}=\beta\left(\frac{FM_{hov}-FM^*}{FM^*}\right)\\+(1-\beta)\left(\frac{\eta_{cr}-\eta^*}{\eta^*}\right)\end{aligned} \tag{19}$$

Regarding the aeroacoustic performance requirements, the optimization must consider noise characteristics under both hover and forward flight conditions. Since lower sound pressure levels indicate better noise performance, the corresponding objective function utilizes the percentage reduction below the target A-weighted sound pressure level (SPL_A) values, again avoiding absolute value metrics. The formulation of this acoustic objective function is shown as Eq. 20. Reference 8 shows that SPL_A in hover condition is much higher than SPL_A in forward flight conditions. Therefore, a higher noise weighting is assigned to the hover condition.

$$f_{acoustic} = \gamma\left(\frac{SPL^*_{Ahov} - SPL_{Ahov}}{SPL^*_{Ahov}}\right) + (1-\gamma)\left(\frac{SPL^*_{Acr} - SPL_{Acr}}{SPL^*_{Acr}}\right) \quad (20)$$

The wind resistance capability of the rotor must account for both the frequency and intensity of gusts. In the constraints section, the impact of a 10 m/s wind on rotor lift has already been limited. Therefore, the objective function focuses solely on the influence of gust frequency. The reduced frequency k_g (Eq. 21)is employed to characterize the effect of gust frequency on rotor aerodynamics. A high reduced frequency indicates the presence of significant unsteady aerodynamic forces induced by the gust.

$$k_g = \frac{\pi f_g c_{75}}{v_{tip)75}} \quad (21)$$

The wind-related objective function (Eq. 22) is defined as follows:

$$f_{wind} = \frac{k^*_g - k_g}{k^*_g} \quad (22)$$

5.3 Optimal Method

Genetic algorithms (GAs) present distinct advantages despite their relatively longer computation time. As a derivative-free optimization method, GAs can handle diverse objective functions without requiring auxiliary information. The algorithm's inherent parallelism and independence from previous iterations enhance computational efficiency through parallel implementation. Most importantly, the population-based search mechanism of GAs provides superior global exploration capability, significantly reducing the probability of becoming trapped in local optima. These characteristics make GAs particularly suitable for solving complex, multimodal optimization problems with multiple design variables.

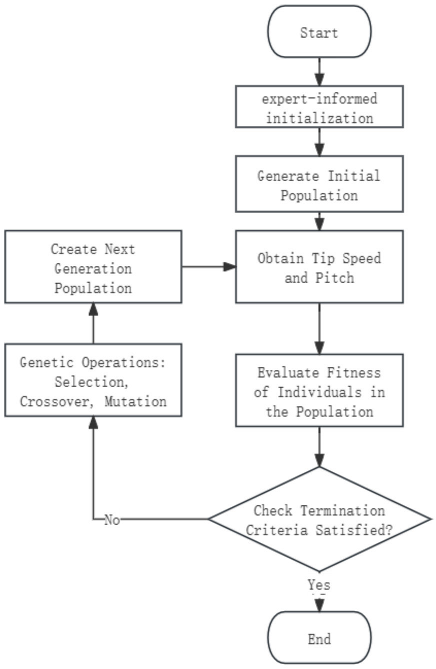

Figure 8: Flowchart of the optimization process

To ensure that the rotor generates sufficient lift and thrust under both hover and forward flight conditions, the tip speed and collective pitch must be adjusted for each flight mode once the aerodynamic shape parameters are specified. Since different combinations of tip speed and collective pitch can yield the same target lift, an optimization approach is required to identify the combination that maximizes overall rotor performance.

Directly treating tip speed and collective pitch as optimization variables in a genetic algorithm increases the dimensionality of the problem. Moreover, the inherent randomness of mutation and crossover in genetic algorithms further elevates the computational burden. Noting that blade geometric parameters and control variables can be decoupled, a two-step optimization framework is adopted, as illustrated in Fig. 3. After each new population is generated by the genetic algorithm, the optimal combination of tip speed and collective pitch for the current blade shape is determined based on gradient information. The rotor performance under this combination is then evaluated and used as the fitness value in the subsequent genetic optimization process.

5.4 Optimal Results

Two sets of optimizations were performed using the proposed method. In the first set, wind resistance capability of the rotor was not considered, i.e., the weighting coefficients satisfied $\alpha_{aero} + \alpha_{acoustic} = 1$, yielding Result A. In the second set, the ratio between α_{aero} and $\alpha_{acoustic}$ was kept constant, but their absolute values were reduced to introduce a wind resistance ability term, resulting in Result B. The second set shares the same ratio between α_{aero} and $\alpha_{acoustic}$ as the first set, but their absolute values are reduced to incorporate the wind resistance coefficient, resulting in Optimization Result B.

The results are compared with the chord distribution of the ATB, as shown in Fig. 9. The chord length of Result A is significantly larger than that of the other two cases, indicating that increasing the chord length while reducing the tip speed can effectively enhance both aerodynamic and acoustic performance. This outcome may be attributed to the lower noise generated by the adopted chord distribution. Since the blade tip has a higher linear velocity, it tends to produce more noise. Therefore, in Result B, the chord length at the tip is moderately reduced, with compensation applied to the mid-span region of the blade.

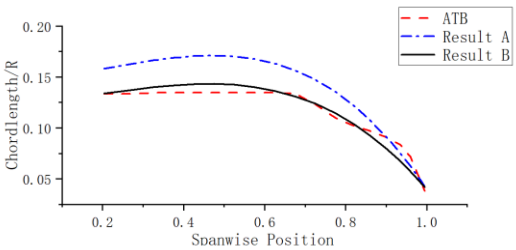

Figure 9: Chord distribution

The results are compared with the twist distribution of the ATB, as shown in Fig. 10. It can be observed that the twist distributions of Result A and Result B are generally smoother than that of the ATB. This is likely because the present optimization method targets variable-speed rotors, which can adjust their inflow conditions by varying the rotational speed, thereby reducing the need for large twist angles.

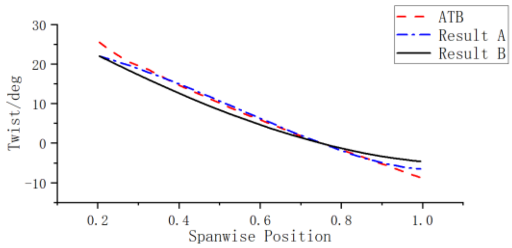

Figure 10: Twist distribution

Unlike the ATB, Result A and Result B exhibit relatively constant twist angles at the blade tip region. This may be attributed to the fact that the computational model accounts for tip vortex effects: near the blade tip, the vortex induces an upward velocity, whereas closer to the inboard section of the tip region, a downward induced velocity is generated. As a result, the combined effect leads to a nearly uniform requirement for twist in this region.

The figure of merit (FM) for each rotor blade is presented in Fig. 11. Within the thrust range of 2500 N to 4500 N, both Result A and Result B exhibit higher FM values than the ATB, with Result B achieving the highest performance. As a result, incorporating wind resistance capability into the optimization may have indirectly improved the rotor's hover performance as well.

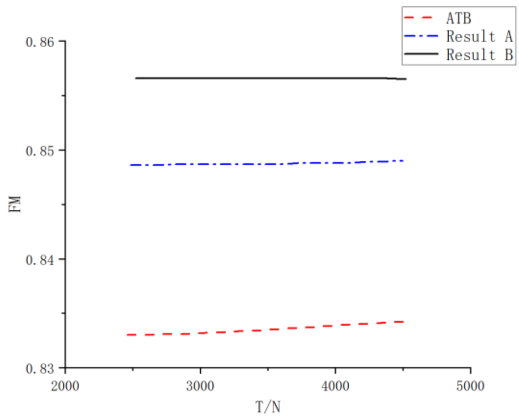

Figure 11: FM at different thrust levels.

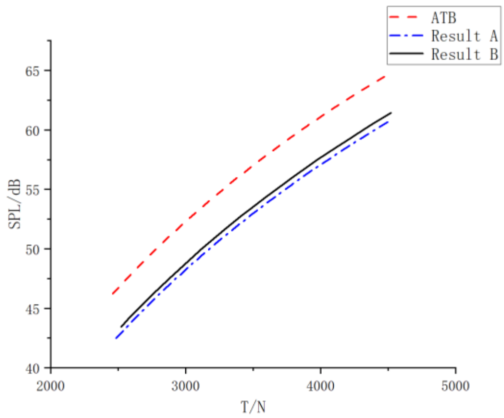

Figure 12: SPL at different thrust levels.

The noise levels of each rotor in helicopter mode are shown in Fig. 12. Within the thrust range of 2500 N to 4500 N, Result B generates approximately 3 dB less noise compared to the ATB blade, while Result A exhibits even lower noise levels. This reduction can be attributed to the lower tip speeds of Result A and Result B, which are 10 to 15 m/s lower than that of the ATB blade when generating equivalent lift and the optimal FM.

Energy consumption is also a critical factor in rotor design. Under helicopter mode, the total power required by each rotor to generate the same amount of lift is shown in Fig. 13. Results A and B exhibit lower power requirements, which is consistent with the FM results, indicating that the optimized designs achieve reduced energy consumption in helicopter mode.

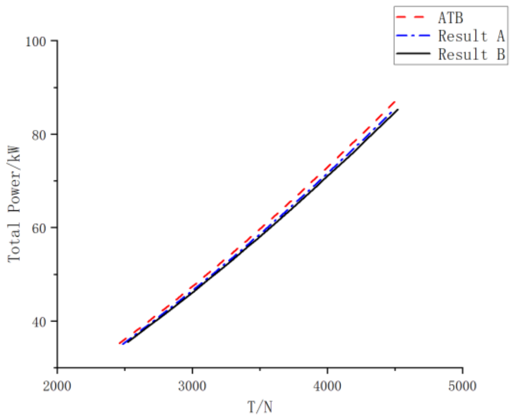

Figure 13: Total Power at different thrust levels.

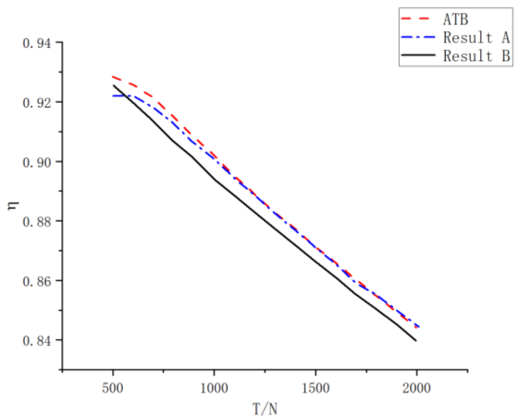

Figure 14: η at different thrust levels.

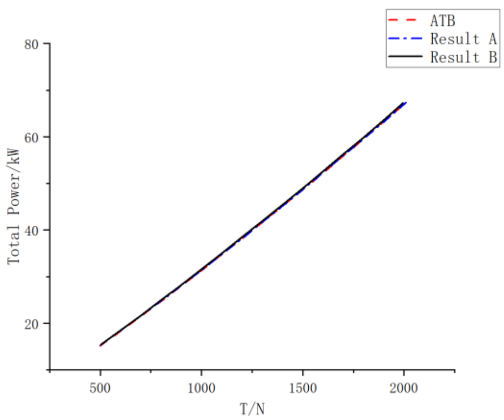

Figure 15: Total power at different thrust levels.

In airplane mode, the variation of propeller efficiency (η) with thrust is shown in Fig. 14. Propeller efficiency of Result A is comparable to that of ATB, while Result B exhibits slightly lower η. Nevertheless, it still maintains a relatively high level of efficiency.

The total power consumption of the rotors in airplane mode is shown in Fig. 15. As illustrated, although Result B exhibits slightly lower propeller efficiency, its impact on the overall power consumption is negligible.

The sound pressure level (SPL) in airplane mode is shown in Fig. 16. As thrust exceeds 1000 N, Result A exhibits lower noise levels. In contrast, Result B shows higher SPLs compared to the other two designs. At 500 N thrust, its SPL is approximately 2 dB higher, and the noise increase reaches up to 6.5 dB as thrust rises to 2000 N. However, since cruise flight occurs at higher altitudes and the overall noise level is relatively low, this increase in SPL remains within an acceptable range.

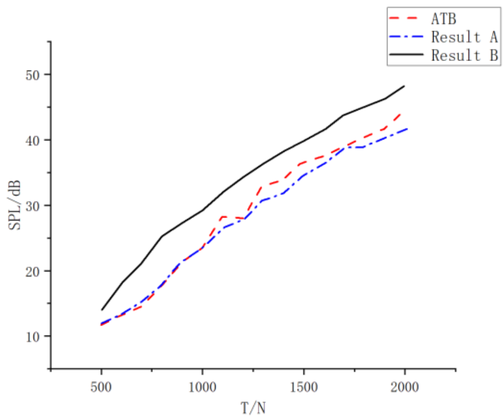

Figure 16: SPL at different thrust levels.

The thrust fluctuation rate ($\Delta T / T$) under a 10 m/s wind in airplane mode is shown in Fig. 17. During the cruise phase at 500 N thrust, Result B exhibits a lower thrust fluctuation rate compared to the other two rotors, indicating superior wind resistance capability. As thrust increases, the fluctuation rate of the ATB rotor decreases sharply and, at certain thrust levels, becomes lower than that of Result B. However, the ATB rotor also shows larger variations in fluctuation rate. Since the increasing thrust phase typically corresponds to accelerated climb, such fluctuations may impose additional control burdens on the aircraft.

From Result A, without considering wind resistance capability, it is evident that increasing solidity and reducing tip speed can enhance rotor performance. Compared to the ATB, Result A improves FM by 1.7%, reduces SPL in hover by approximately 4 dB, and maintains nearly the same propeller efficiency (η). Additionally, it achieves a 0–2 dB SPL reduction during forward flight.

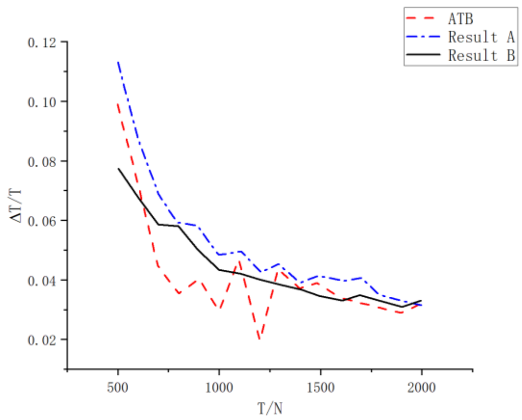

Figure 17: Thrust fluctuation rate at different thrust levels.

Result B demonstrates that introducing a wind resistance coefficient effectively improves rotor thrust stability under gust conditions. The thrust fluctuation rate is reduced by 21.8% compared to the ATB, and the rate remains smoother across varying thrust levels. A lower gust reduced frequency (k_g) also indicates better resistance to unsteady aerodynamic loads.

Specifically, Result B increases FM by approximately 2.7% and reduces hover SPL by about 3 dB compared to the ATB. Although η is reduced by roughly 0.5%, the change in total power consumption is negligible. During the cruise, the SPL is 2–4 dB higher than that of the ATB. During the cruise phase, the SPL is relatively low, and the aircraft remains at a considerable distance from the ground while passing quickly over fixed locations. As a result, the incremental noise remains within an acceptable range.

6. CONCLUSION

This study employs a comprehensive analysis code to investigate the effects of various parameters on the performance of variable-speed rotors. Based on these results, the ranges and constraints for the optimization variables are defined. To improve computational efficiency, the proposed optimization method decouples blade geometry parameters from tip speed. In response to the typical wind resistance capability of eVTOLs, a wind resistance coefficient is incorporated into the objective function. Two optimization rounds were conducted: Result A corresponds to the case without wind resistance capability considerations, while Result B includes wind resistance as part of the optimization objective.

The following conclusions can be drawn:

1. Variable-speed rotors can maintain optimal figure of merit (FM) across a wide thrust range by adjusting tip speed and collective pitch, offering greater design flexibility.
2. Both Result A and Result B exhibit smaller variations in twist angle compared to the ATB. This is likely because variable-speed rotors can coordinate changes in rotational speed and collective pitch to trim lift, thereby reducing the need for large twist to accommodate variations in inflow speed and direction.
3. Enhancing wind resistance also indirectly improves the rotor's aerodynamic performance in hover. However, this comes at the expense of noise and cruise performance. Result B thus suggests that sacrificing some cruise noise performance in exchange for enhanced wind resistance is a viable design trade-off.
4. This optimization method ensures constant thrust and nearly unchanged total power, making it applicable to scenarios where external constraints, such as motor characteristics, remain fixed.

Author contact:

Tianheng Yao	yaotianhengpku@gmail.com
Yiran Gong	yrgong@outlook.com
Liangjun Li	liliangjun2006@126.com
Shuai Zhang	zhangs23@mails.tsinghua.edu.cn
Chen Jiang*	jc2017@mail.tsinghua.edu.cn
Haowen Wang	bobwang@tsinghua.edu.cn

7. REFERENCES

1. Li, B., Li, C., Yang, Q., Tian, Y., and Zhang, X., *"Full-Scale Wind Speed Spectra of 5-Year Time Series in Urban Boundary Layer Observed on a 325 m Meteorological Tower," Journal of Wind Engineering and Industrial Aerodynamics*, Vol. 218, 2021, Paper No. 104791.

2. Jones, A.R., Cetiner, O., and Smith, M.J., *"Physics and Modeling of Large Flow Disturbances: Discrete Gust Encounters for Modern Air Vehicles," Annual Review of Fluid Mechanics*, Vol. 54, No. 1, 2022, pp. 469–493.

3. Narayanan, S., and Govindarajan, B., "Effects of Gust on the Aerodynamics of Multi-Rotors," *Physics of Fluids*, Vol. 36, (12), Dec. 2024, Article

No. 127169. DOI: 10.1063/5.0243421.

4. Morgado, J., Abdollahzadeh, M., Silvestre, M.A.R., and Páscoa, J.C., *"High Altitude Propeller Design and Analysis," Aerospace Science and Technology*, Vol. 45, 2015, pp. 398–407.

5. Stajuda, M., Karczewski, M., Obidowski, D., and Jóźwik, K., *"Development of a CFD Model for Propeller Simulation," Mechanics and Mechanical Engineering*, Vol. 20, No. 4, 2016, pp. 579–593.

6. Clarke, M.A., and Botero, E., "Aeroacoustic Optimization of VTOL Rotor Blades," *AIAA SciTech 2023 Forum*, Jan. 2023. DOI: 10.2514/6.2023-0209.

7. Wilke, G., Bailly, J., Kimura, K., and Tanabe, Y., "JAXA-ONERA-DLR Cooperation: Results from Rotor Optimization in Hover," *CEAS Aeronautical Journal*, Vol. 13, (2), Apr. 2022, pp. 313–333. DOI: 10.1007/s13272-022-00580-8.

8. Pascioni, K.A., Watts, M.E., Houston, M.L., Lind, A.H., Stephenson, J.H., and Bain, J.J., "Acoustic Flight Test of the Joby Aviation Advanced Air Mobility Prototype Vehicle," *28th AIAA/CEAS Aeroacoustics 2022 Conference*, Paper No. 3036, Jun. 2022. DOI: 10.2514/6.2022-3036.

9. Stoll, A.M., "Design of Quiet UAV Propellers," Engineer's thesis, Stanford University, June 2012.

10. Xiang, S., Liu, Y.-Q., Tong, G., Zhao, W.-P., Tong, S.-X., and Li, Y., "An Improved Propeller Design Method for the Electric Aircraft," *Aerospace Science and Technology*, Vol. 78, (12), Jul. 2018, pp. 488–493. DOI: 10.1016/j.ast.2018.05.008.

11. Adkins, C.N., and Liebeck, R.H., "Design of Optimum Propellers," *Journal of Propulsion & Power*, Vol. 10, (5), Sept.–Oct. 1994, pp. 676–682. DOI: 10.2514/3.23779.

12. Pinto, O.L., Bossotto, G., Afonso, F., and Lau, F.P., "On Rotor Aeroacoustic Optimization for Urban Air Mobility," *28th AIAA/CEAS Aeroacoustics 2022 Conference*, Paper No. 2022-2946, Jun. 2022. DOI: 10.2514/6.2022-2946.

13. Lenfers, C., Janssen, R., Beck, N., Friedrichs, J., and Rezaeian, A., "Experimental Investigation of the Propeller Design for Future QESTOL Aircraft in the BNF Project," *AIAA SciTech Forum and Exposition, 52nd Aerospace Sciences Meeting*, Paper No. 2014-0562, Jan. 2014. DOI: 10.2514/6.2014-0562.

14. Leishman, J.G., and Bagai, A., "Fundamental Studies of Rotor Wakes in Low Speed Forward Flight Using Wide-Field Shadowgraphy," *AIAA Paper 91-3232*, Jan. 1991. (Conference paper, no traditional journal/volume/pp.)

15. Farassat, F., "Derivation of Formulations 1 and 1A of Farassat," *NASA Technical Memorandum NASA/TM-2007-214853*, March 2007.

16. Vatistas, G.H., Kozel, V., and Mih, W.C., "A Simpler Model for Concentrated Vortices," *Experiments in Fluids*, Vol. 11, (1), Apr. 1991, pp. 73–76. DOI: 10.1007/BF00198434.

17. Johnson, W., "Helicopter Theory," *Helicopter Theory*, Courier Corporation, North Chelmsford, MA, Mar. 2012.

18. Althoff, S.L., Elliott, J.W., and Sailey, R.H., "Inflow Measurements Made with a Laser Velocimeter on a Helicopter Model in Forward Flight. Volume 1: Rectangular Planform Blades at an Advance Ratio of 0.15," *NASA Technical Memorandum NASA/TM-100541*, Apr. 1988.

19. Brentner, K.S., "Prediction of Helicopter Rotor Discrete Frequency Noise: A Computer Program Incorporating Realistic Blade Motions and Advanced Acoustic Formulation," *NASA Technical Memorandum NASA/TM-87721*, Oct. 1986.

20. Harris, F.D., "Hover Performance of Isolated Proprotors and Propellers—Experimental Data," *NASA Contractor Report NASA/CR-2017-219486*, Dec. 2017.

21. Traub, L.W., Botero, E., Waghela, R., Callahan, R., and Watson, A., "Effect of Taper Ratio at Low Reynolds Number," *Journal of Aircraft*, Vol. 52, (3), May 2015, pp. 734–747. DOI: 10.2514/1.C032559.
22. Vatistas, G.H., Kozel, V., and Mih, W.C., "A Simpler Model for Concentrated Vortices," *Experiments in Fluids*, Vol. 11, (1), Apr. 1991, pp. 73–76. DOI: 10.1007/BF00198434.

8. CLASSIFICATION & COPYRIGHT

The paper must be unclassified for release to the public and cleared by the appropriate company and/or government agency if necessary. CEAS and its national member societies shall be allowed to publish the paper. The copyright information is stated on the Forum website https://www.rotorcraft-forum.eu/ and on the front page of this template. All papers presented at the ERF will be published as ERF proceedings. In addition they will be available in a freely accessible web-based repository 2 years after the respective conference.